The International Journal of Advanced Manufacturing Technology (2023) 129:3475–3483
https://doi.org/10.1007/s00170-023-12535-2

ORIGINAL ARTICLE

In-process thermal imaging to detect internal features and defects in fused filament fabrication

Youssef AbouelNour[1] · **Nikhil Gupta**[1]

Received: 14 July 2023 / Accepted: 17 October 2023 / Published online: 27 October 2023

Abstract
The objective of this work is to identify and measure in situ the embedded features in parts manufactured with a fused filament fabrication (FFF) 3D printer. After implementing the monitoring system consisting of optical and thermal cameras, the efficiency of the system is determined in terms of efficacy for automated defect detection through data analysis. In contrast to our previous work, which involved the detection of a large number of randomly embedded sub-surface defects, this study identifies defects of various sizes, geometries, and depths printed in a rectangular strip. Temperature differences, or ΔT, between certain layers are evaluated to determine their significance to the detection of embedded features and internal voids. ΔT between the final layer of a void within the embedded feature and the subsequent layer was found to increase as void size decreased. ΔT between the formation layer and the subsequent layer decreased as void size decreased. Additionally, embedded feature geometries registered higher ΔT between formation layer and the subsequent layer when they consisted of 3-layer voids, which indicates that larger voids, or multilayer defects, within embedded features led to higher formation layer temperatures. Overall, real-time image acquisition, image processing, and data correlation was demonstrated to effectively detect abnormalities in large datasets.

Keywords In situ monitoring · Additive manufacturing · Thermal imaging · Defect detection · Embedded features

1 Introduction

In situ imaging and non-destructive testing (NDT) methods have been extensively used in additive manufacturing (AM) for process monitoring, quality monitoring, and more recently, in-process defect detection [1]. Studies have used techniques such as ultrasonic testing to detect embedded internal features in AM [2, 3]. Other studies have used imaging methods such as optical scanners and IR thermography to visualize internal features and detect embedded defects [4–7]. Thermal cameras work by measuring the surface temperature of the build material and can provide valuable insights into the melting, solidification and cooling process [8, 9]. For instance, a thermal camera can detect variations in temperature that may indicate the onset of defects and relate it to the energy input into the build material to help optimize the processing parameters [5, 10, 11].

Developing an efficient in situ monitoring method requires determining the system resolution in terms of the minimum detectable feature size, the effects of feature size on the monitoring methods, and the capabilities of detecting defects of different shapes, sizes, and orientations. However, there is a lack of literature regarding detection of multilayer defects in printed geometries. Extrusion-based AM processes are a cost-efficient way to develop parts with complex geometries and large build volumes [12]. These processes typically utilized polymeric materials for printing [13]. Recent advancements have allowed for the use of a wider range of materials such as metallic materials, ceramics, and other construction materials, which has broadened the use of extrusion-based processes, such as fused filament fabrication (FFF) [14].

In this work, features of various geometries are embedded inside specimens printed using FFF that are monitored in situ using infrared (IR) camera. Parameters such as minimum allowable feature size and feature shape are evaluated with respect to 3D printer tolerances and resolution of the

✉ Youssef AbouelNour
ywa201@nyu.edu

[1] Composite Materials and Mechanics Laboratory, Mechanical and Aerospace Engineering Department, New York University, Tandon School of Engineering, 6 MetroTech Center, Brooklyn, NY 11201, USA

in situ monitoring system. Temperature variation monitoring is used to determine the effects of feature size and shape on detection accuracy. By evaluating temperature profiles of specific layers within the embedded feature geometries, it is evident that temperature variation monitoring can be used for feature detection, multilayer defect detection, and evaluation of 3D printer capabilities.

2 Materials and methods

Hollow internal features were embedded in a 53 × 13 × 5 mm rectangular strip. The features, shown in Fig. 1, consisted of four different shapes of three different depths each to constitute twelve configurations. Figure 1a and b show the rectangular strip with the features in the CAD file created in SolidWorks and the geometries sliced using Ultimaker Cura 4.9.1, respectively. Figure 1c and d show front views of the specimen. As pictured in Fig. 1e, the hollow features, from left to right, included 3 small square prisms (SSP), 3 large square prisms (LSP), 3 triangular prisms, and 3 cylinders.

Table 1 provides dimensions of the top face of each feature, where *b* is the base, *h* is the height, and *d* is the diameter. Note, due to 3D printer tolerances and nozzle diameter, Cura interpreted the triangular prism geometry into a diamond prism. The three features of the same geometry, Fig. 1e and f had different depths of 0.2, 0.4, and 0.6 mm corresponding to the numbers 1, 2, and 3 marked in the figures, which ensured 1, 2, or 3 layers of these features due to the layer height of 0.2 mm. Each feature's edges enclosed 1–3 layers of space.

A Prusa MK3 3D Printer was used to print all specimens. Print speed of 80 mm/s, print bed and nozzle temperatures of 60 °C and 210 °C, respectively, and default settings for other printing parameters—i.e., infill, extruder travel, material flow, and material temperature—were applied. A three-layer raft was created to avoid warping, giving a total of 28 layers. The in situ monitoring method used in this work resembled that introduced in our previous publication [7]. Timelapse was enabled to move the extruder to a specified location after a layer was completed and pause the print for 5 s, during which optical and thermal images were captured.

Void formation within the hollow features served as initiation of 1-, 2-, or 3-layer defects within the feature geometries, creating multilayer defects in the printed specimens. Figure 2 shows the sequence of formation of different features and the voids within them as various layers of the specimen are printed. Standard layer printing resumed after the features were printed. A summary of this process is given in Table 2. Table 3 lists the actual sizes of embedded features in the printed specimens measured after sectioning of printed specimens.

Similar to [7], FLIR E5-XT infrared (IR) camera was used for thermal imaging. It captures radiometric images

Table 1 Dimensions of the top face of each internal feature

Top face	Dimensions
Small square	0.5 mm × 0.5 mm
Large square	1 mm × 1 mm
Triangle	$b = 1$ mm; $h = 0.867$ mm
Circle	$d = 1$ mm

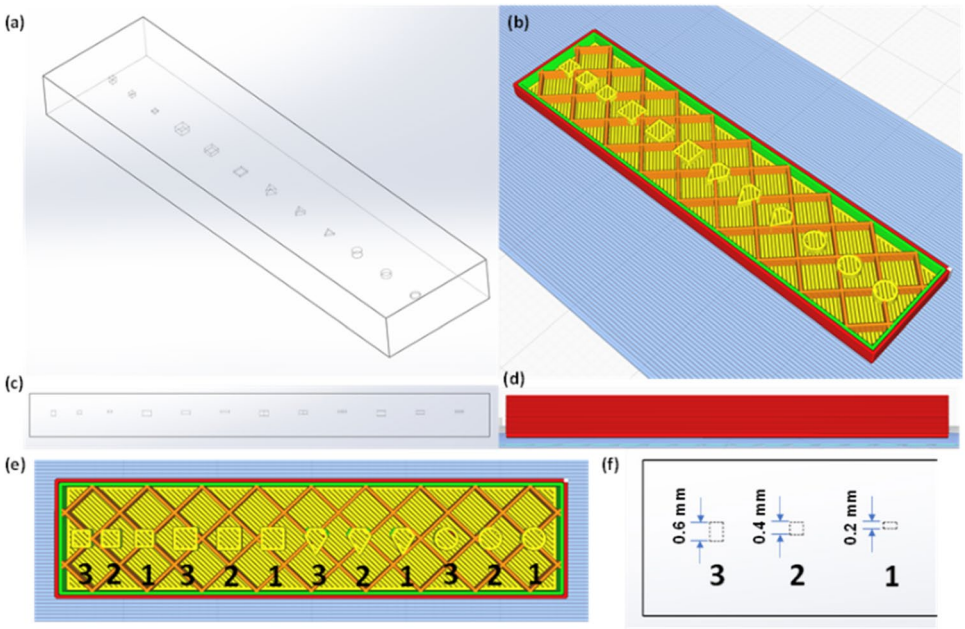

Fig. 1 Rectangular strip showing embedded hollow features. **a**) Isometric view in SolidWorks, **b** isometric view in Cura, **c** front view in SolidWorks, **d** front view in Cura, **e** top view in Cura showing feature sets, and **f** sectioned front view in SolidWorks showing feature heights

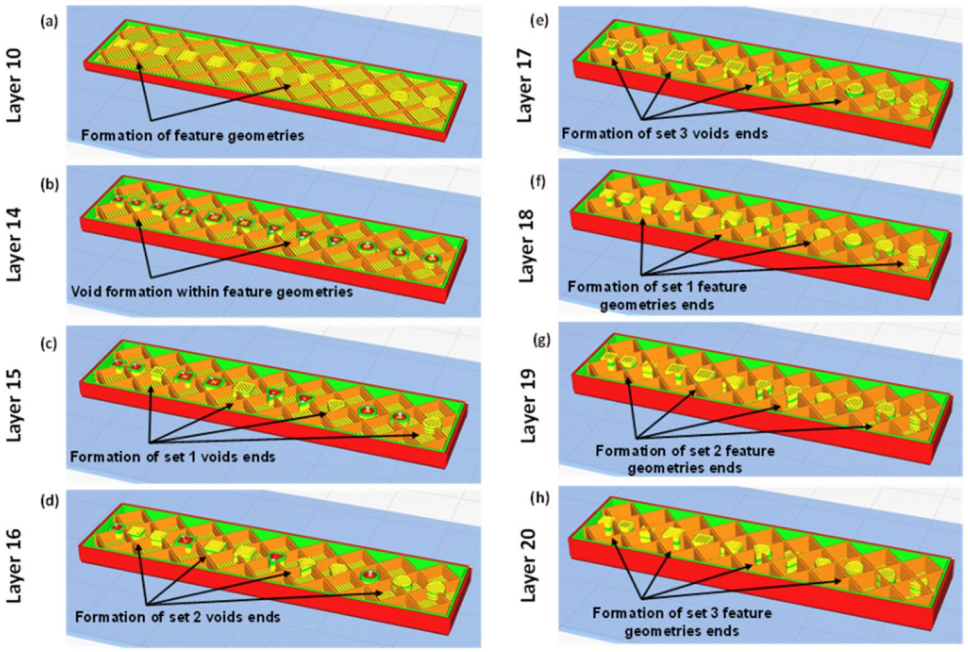

Fig. 2 Isometric views of rectangular strip in Cura showing **a** formation of different feature geometries, **b** void formation within feature geometries, **c** end of set 1 void formation, **d** end of set 2 void formation, **e** end of set 3 void formation, **f** end of set 1 feature geometry formation, **g** end of set 2 feature geometry formation, and **h** end of set 3 feature geometry formation

Table 2 Initiation of embedded hollow features and internal voids

Set no.	Start of geometry: layer 10	End of geometry: layer no.	No. of layers in feature geometry	No. of hollow layers in feature
1	10	18	9	1
2	10	19	10	2
3	10	20	11	3

Table 3 Actual embedded feature sizes

Top face	Dimensions
Small Square	1.67 mm × 1.67 mm
Large Square	2.40 mm × 2.40 mm
Triangle	$b = 2.40$ mm; $h = 2.10$ mm
Circle	$d = 2.40$ mm

at a frequency of 9 Hz and a resolution of 19,200 (160 × 120) pixels with a spectral range of 7.5–13 µm, an extended temperature range of − 20–400 °C and a resolution of 0.001 °C. The camera is capable of capturing both thermal and optical images, as well as producing fused images using its proprietary technology, FLIR MSX®, or the Multi-Spectral Dynamics Imaging tool. Pictured in Fig. 3, the IR camera was mounted onto a flexible stand in front of the printer and focused downward at the build plate, aligned with the printer's *y*-direction belt. Images of the specimens on the heated build plate were captured within 2 s after completion of each layer, ensuring consistency of temperature profiles in the thermal images.

FLIR's online database was used to calculate the camera's field of view. Temperature accuracy was confirmed by assessing actual and measured print bed temperatures. The reflected apparent temperature was set to 20 °C. Specimens were printed using polylactic acid (PLA). The emissivity of PLA was set to 0.95 throughout the experiments [15]. The printer and IR camera were both calibrated upon system startup and prior to each new trial run.

Five trial runs were conducted to assess the reliability of the experimental procedure. The acquired thermal image sets were processed and analyzed using FLIR Thermal Studio Pro. This included fusion alignment, color gradient adjustment, isotherm management, spotmeter temperature measurements, emissivity measurement and adjustment, and other spatial measurements. For temperature variations analysis, spotmeter temperature measurements were first gathered from thermal image sets. Spotmeter temperature measurements were taken at the twelve locations at which features were embedded in the rectangular strip. These locations are marked in Fig. 4 as S1–S12. As pictured in Fig. 4b–g, these are also locations where a separation of colors is evident due to the formation of embedded features with internal voids, which categorizes them as *hotspots* [7]. In this work, *hotspot* temperatures ranged from around 50 to 66 °C.

Batch processing was conducted for temperature measurements at the predetermined locations in the thermal image sets. The algorithm, shown in Fig. 5, created a separate file for each temperature measurement in a thermal image set. Python was then used to create a script that created a .csv

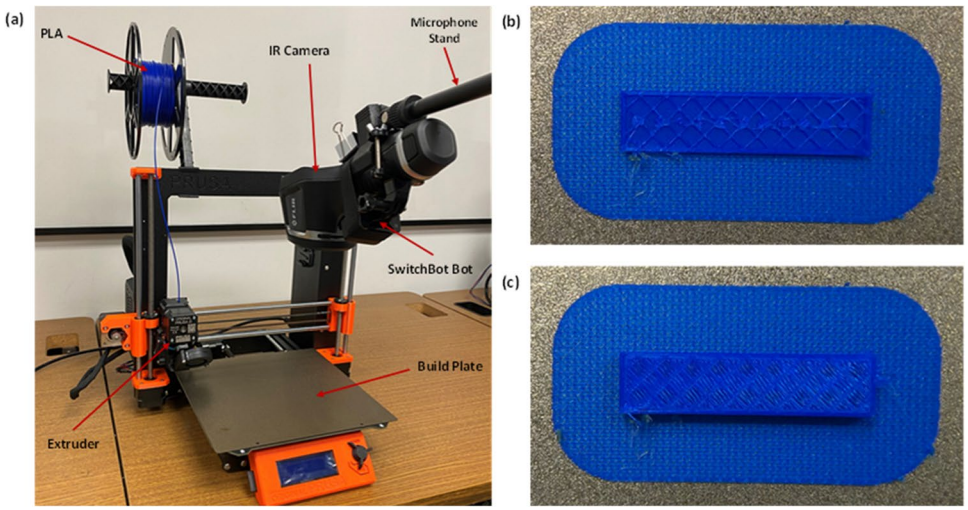

Fig. 3 **a** In situ monitoring system for IR thermal imaging and optical images of **b** layer 10 and **c** layer 25 of the printed specimen

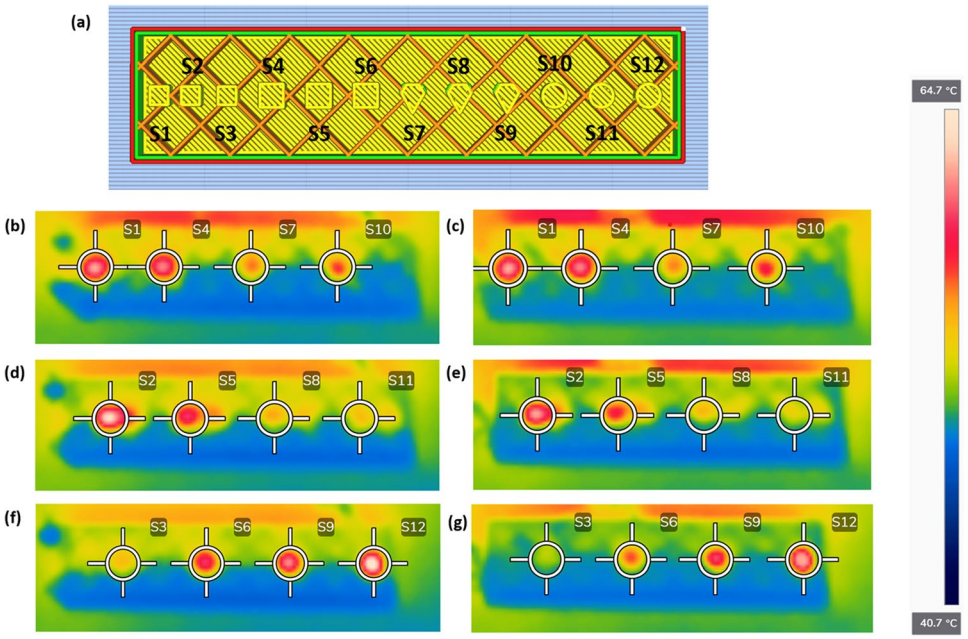

Fig. 4 Spotmeter temperature measurement locations (**a**) sliced layer and (**b**–**g**) thermal images showing elevated temperatures. As feature location differs in each layer, spotmeter measurement location also differed

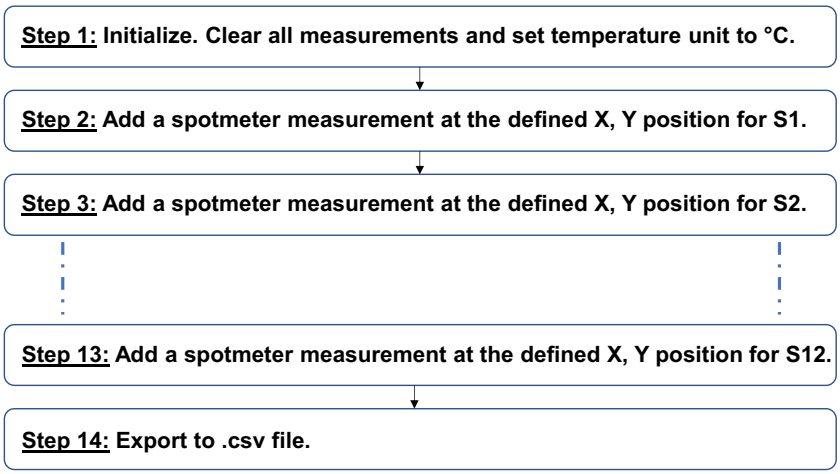

Fig. 5 Batch processing algorithm created in FLIR Thermal Studio Pro

file consisting of 28 rows and 12 columns of temperature measurements in ascending order based on layer and spot temperature measurement, respectively. Python scripts were created to obtain specific parameters for each defect set as shown in Fig. 6 to analyze the effects of embedded features and internal voids on temperature variations in the printed AM specimens. The low thermal conductivity of air compared to PLA, 2.6–6.7 × 10^{-2} W m^{-1} K^{-1} and 16.0 × 10^{-2} W m^{-1} K^{-1}, respectively, was considered when analyzing the results [7].

3 Results

The trends interpreted from the acquired parameters led to several conclusions on the effects of feature shape, size, and core structure on temperature variations in the AM specimens. As shown in Fig. 7a, the temperature difference (ΔT) between the final layer of a void and the subsequent layer enclosing the void increased from a SSP to LSP to diamond prism to cylinder for a 1-layer void in the hollow geometries by 158, 31, and 29%, respectively. However, it was found that ΔT decreased from SSP to LSP to diamond prism or cylinder by 19, 46, and 25% for 2-layer and 14, 60, and 12% for 3-layer voids. Additionally, for the diamond prism and cylinder, 1-layer internal voids resulted in significantly greater ΔT between the final layer of the void and the subsequent layer compared to 2- and 3-layer voids with ΔT of 8.53 and 11.01 °C, respectively. For the diamond prism, it was 144 and 306% greater for a 1-layer void than 2- and 3-layer voids, respectively. For the cylinder, it was 321 and 367% greater for a 1-layer void than 2- and 3-layer voids, respectively. For the LSP, ΔT between the final layer of the voids and the subsequent layer was within a similar range of 5–6.67 °C, while for the SSP, it decreased from a 2- to 3- to 1-layer void, and

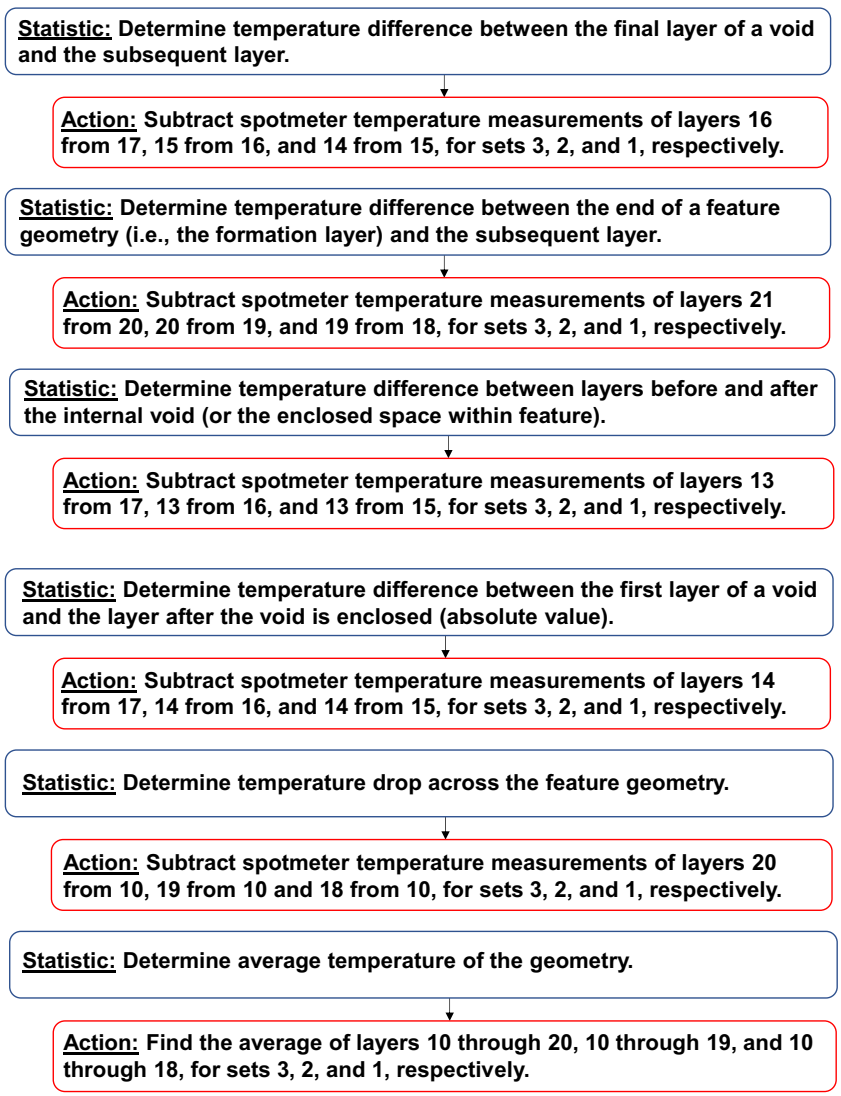

Fig. 6 Parameters obtained from data sets for temperature variations monitoring with respective actions performed in developed Python scripts for acquisition

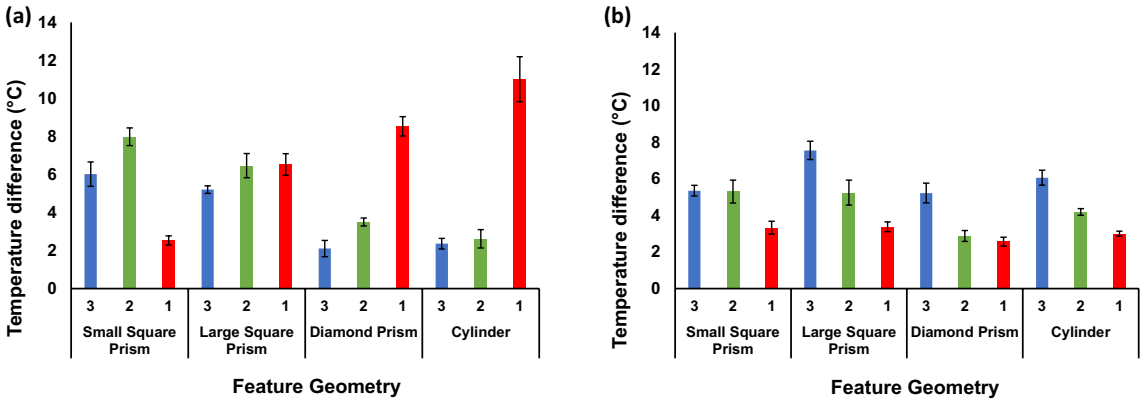

Fig. 7 **ΔT** between **a** the final layer of a void (i.e., 1-, 2-, and 3-layer) and the subsequent layer and **b** the formation layer and the subsequent layer for the four different geometry types

therefore, measurements were inconsistent compared to other geometries.

As shown in Fig. 7b, ΔT between the end of a feature geometry, or formation layer, and the subsequent layer decreased as void size decreased for every geometry type. For a SSP, ΔT decreased by 1 and 37% from a 3- to 2-layer void and from a 2- to 1-layer void, respectively. For a LSP, ΔT decreased by 31 and 36% from a 3- to 2-layer void and from a 2- to 1-layer void, respectively. Similarly, for a diamond prism, ΔT decreased by 45 and 11% and for a cylinder, by 31 and 28%. ΔT was least between the formation layer and the subsequent layer overall for the diamond prism.

Other measured parameters concerning temperature variation surrounding the internal void within the hollow features were evaluated. For ΔT between layers before and after an internal void, or in other words, those within the enclosed spaces in the hollow features, there were mixed correlations for the different feature geometries and void depths. However, it was evident that ΔT was higher for SSPs followed by LSPs for all void depths, and more than 50% lower for diamond prisms and cylinders. For ΔT between the first layer of a void and the layer printed to enclose the void, there was a positive correlation for a 1-layer void from SSP to LSP to diamond prism to cylinder, but a negative correlation for a 2- and 3-layer void from SSP to LSP to cylinder to diamond prism. Therefore, it is evident that temperature variations within an embedded feature can give relevant information about void depth through the following statistic. A defect that is more than one layer thick can be detected through temperature variations analysis.

Average temperatures ($\widetilde{T}$) of the embedded features and temperature drops across the features were also obtained as shown in Fig. 8. $\widetilde{T}$ of a hollow embedded feature geometry was greatest for a SSP and lowest for a diamond prism, decreasing in order from SSP to LSP to cylinder to diamond prism. For temperature drops across the embedded feature geometries, it was found that for a 1-layer void, it was greatest for a cylinder, while for 2- and 3-layer voids, it was greatest for a SSP followed by an LSP.

4 Discussion

Six parameters were evaluated in an attempt to determine the relevance of each parameter to feature detection and the effects of temperature variations on the detection of multilayer defects. By embedding 1-, 2-, and 3-layer voids within the feature geometries, hollow features were created. Void formation resembled multilayer defect formation within the printed specimens. This allowed for studying the effects of temperature variations on both embedded features and multilayer defects. Although embedded features are designed with specific dimensions, they are most likely subject to limitations by 3D printer and material tolerances, meaning feature size may be decreased in actuality. The Prusa MK3 has tolerances of around 0.3 mm on the x- and y-axis and 0.1 mm on the z-axis. Measuring actual embedded feature size confirmed limitations due to the 3D printer's tolerances and assisted in acknowledging the actual resolution of the in-situ monitoring system used in this work. It was found that for a designed feature size < 1 mm, there was a 240–330% increase in printed feature size. For a designed feature size of 1 mm, there was a 240% increase in printed feature size. It is estimated that a designed feature size of 2.4 mm would result in an accurate actual feature size. Tolerances also restricted formation of the triangular prism designed in the 3D model. Diamond prisms formed instead with the minimum allowable feature size for formation. This section will reference the actual embedded feature sizes.

ΔT between the final layer of a void and the subsequent layer showed a common trend in the dataset for a minimum feature size. For a LSP, diamond prism, and cylinder, all

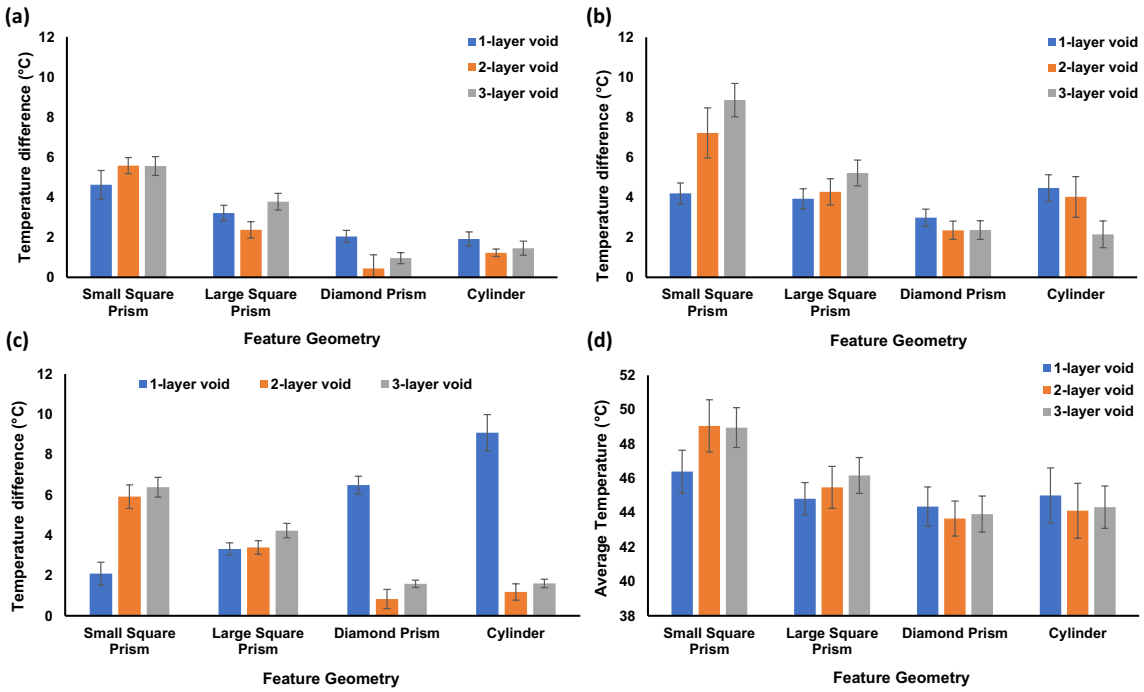

Fig. 8 **a** ΔT within enclosed space in a hollow embedded feature, **b** ΔT across geometry, **c** ΔT between first layer of a void and layer after the void is enclosed, and **d** T of feature geometry for the four different geometry types. Note that the y-axis scale for **d** is different than that of the other figures

with a minimum feature size of 2.4 mm, it was found that ΔT increased from a 3- to a 2- to a 1-layer void. For a SSP, a feature with a size of 1.67 mm, this trend was not found. While a 2.4 mm feature size for a square prism developed a correlation between temperature variations and multilayer defect formation, a 1.67 mm feature size for the same geometry did not. Hence, the spatial resolution of the in-situ monitoring system developed in this work is most likely $>$ 1.67 mm and $\leq$ 2.4 mm due to the limitation of the printer resolution, while the imaging system can likely detect finer defects.

Moreover, 1-layer internal voids resulted in significantly greater ΔT between the final layer of the void and the subsequent layer compared to 2- and 3-layer voids for a diamond prism and a cylinder. With ΔT of 8.53 and 11.01 °C for a diamond prism and cylinder, respectively, it is evident that a 1-layer void can be detected with more certainty for these two geometries with the given feature size compared to 2- and 3-layer voids by measuring ΔT between the final layer of a void and the subsequent layer. This trend was not found for the square prisms. While ΔT decreased from 1- to 2- to 3-layer voids for a LSP, it only showed a small deviation, falling within the range of 5–6.67 °C. For a SSP, a 2-layer void led to a higher ΔT followed by a 3-layer void then a 1-layer void. Square prisms consist of four sharp corners, and therefore, they are more susceptible to deviations from design due to 3D printer tolerances, leading to the trends found. Hence, given a minimum feature size of 2.4 mm, hollow features with 1-layer voids showed greater ΔT between the final layer of a void and the subsequent layer. Since the hollow features consist of 1-, 2-, and 3-layer voids, the temperature measurement of a feature with a hollow layer is that of the cooler, printed material on the last complete layer. As the number of hollow layers in a feature increases, ΔT between the final layer of a void and the subsequent layer decreases, as the final layer of the void actually measures the temperature of the last complete layer, which continues to drop as time is accumulated.

For ΔT between the formation layer and the subsequent layer, as void size decreased, ΔT also decreased for every geometry type. ΔT was greatest for an LSP, followed by a cylinder. Both geometries also registered similar trends, which is likely due to their similar surface areas. Overall, embedded feature geometries registered higher ΔT between formation layer and the subsequent layer when they consisted of 3-layer voids. This indicates that larger multilayer defects within embedded features led to higher formation layer temperatures, and hence, can be detected by measuring ΔT between the formation layer and the subsequent layer. Note that regardless of size, each void was followed by three fully printed layers prior to the end of the geometry, which increased in temperature due to extruded material falling into hollow spaces leading to slower cooling rates. This led to elevated formation layer temperatures.

ΔT within hollow areas in the embedded features, or that between the layers before and after a void, was greatest for the small square prisms. Due to the low thermal conductivity of air compared to PLA, entrapped air in the features leads to great heat retention above the void. As the feature size decreases, the heat retention increases, and thus, ΔT increases. Therefore, results may have shown higher ΔT's within the hollow areas and across the geometry for the SSP due to this reason. ΔT within hollow areas in the embedded features, or that between the layers before and after a void, was least for diamond prisms and cylinders. The temperature of the layer after the void was that of the last complete layer in the feature due to the hollow space in between. Therefore, the small ΔT of 0.44–2.06 °C for the diamond prisms and cylinders confirm our findings for resolution of the in situ monitoring system. Similarly, for ΔT between the first layer of the void and the layer after the void is enclosed, measurements were minimal for 2- and 3-layer voids in diamond prisms and cylinders due to the same reasons. For a 1-layer void, ΔT was around 6.5 and 9.1 °F for a diamond prism and cylinder, respectively. These are indicative of high cooling rates within the printed geometry for the subsequent layer that decrease significantly as additional layers are printed thereafter. For both of these parameters, high ΔT for the square prisms are indicative of the effects of tolerances on the embedded features.

For the diamond prism and cylinder, the temperature drop decreased from 1- to 2- to 3-layer voids, which correlates to results obtained for ΔT between the formation layer and the subsequent layer. Elevated formation layer temperatures indicate smaller temperature drops across the feature geometries. The $\widetilde{T}$ of the geometry was greatest for the SSP for all void sizes, but fell within the range of 43–46 °C for all other geometries and void sizes. Therefore, the significance of the $\widetilde{T}$ of an embedded feature geometry is not evident and would not be indicative of void formation within the features.

Although the camera resolution is much higher, the resolution of the in situ monitoring system was found to be limited to the printer resolution of creating a feature in the print. The effectiveness of the defect detection process in this work depends on factors such as the melting point of the material and the void size, including void depth. The observed temperature difference ranges would shrink for materials with lower melting points. Successful detection also depends on the temporal resolution of the monitoring system. Images must be acquired consistently following layer cooling. Cooling rates may vary depending on the feature geometry and void size. False positives are unlikely to occur in this dataset. However, false negatives may occur due to natural voids within the specimens. This can be overcome by taking more spotmeter measurements at locations where features were not embedded. If elevated temperature values and large temperature differences are observed in these locations, they are likely to be due to natural voids within the specimens or aftereffects of the embedded features.

5 Conclusions

In this work, in situ monitoring of the 3D printed specimens provided novel findings on the effects of feature geometry and internal voids on temperature variations within the specimens. The effects of 3D printer tolerances and monitoring system resolution on the ability to detect features and defects in real-time were also evaluated. Spatial resolution of the in situ monitoring system was limited to the deposition resolution of the printer of 2.4 mm. For an actual minimum feature size of 2.4 mm, it was found that ΔT between the final layer of a void and the subsequent layer increased from a 3- to 2- to 1-layer void. It was also found that for every feature geometry, ΔT between the formation layer and the subsequent layer decreased as void size decreased. Overall, embedded feature geometries registered higher ΔT between formation layer and the subsequent layer when they consisted of 3-layer voids, which indicates that larger voids, or multilayer defects, within embedded features led to higher formation layer temperatures.

Funding This work is supported by the ASNT Fellowship Award 2022 and the National Science Foundation SaTC grant DGE-1931724. The views expressed in this article are those of the authors and not of the funding agencies.

Declarations

Competing interests The authors declare no competing interests.

References

1. AbouelNour Y, Gupta N (2022) In-situ monitoring of sub-surface and internal defects in additive manufacturing: A review. Mater Des 222:111063
2. Pieris D, Stratoudaki T, Javadi Y, Lukacs P, Catchpole-Smith S, Wilcox PD, Clare A, Clark M (2020) Laser Induced Phased Arrays (LIPA) to detect nested features in additively manufactured components. Mater Des 187:108412
3. Yu J, Zhang D, Li H, Song C, Zhou X, Shen S, Zhang G, Yang Y, Wang H (2020) Detection of internal holes in additive manufactured Ti-6Al-4V part using laser ultrasonic testing. Appl Sci 10(1):365
4. Bugatti M, Colosimo BM (2022) The intelligent recoater: A new solution for in-situ monitoring of geometric and surface defects in powder bed fusion. Addit Manuf Lett 3:100048
5. Szymanik B, Psuj G, Hashemi M, Lopato P (2021) Detection and identification of defects in 3D-printed structures via thermographic inspection and deep neural networks. Materials 14(15):4168
6. Hossain R-E-N, Lewis J, Moore AL (2021) In situ infrared temperature sensing for real-time defect detection in additive manufacturing. Addit Manuf 47:102328
7. AbouelNour Y, Gupta N (2023) Assisted defect detection by in-process monitoring of additive manufacturing using optical imaging and infrared thermography. Addit Manuf 67:103483

8. Vavilov V, Burleigh D (2020) Infrared thermography and thermal nondestructive testing. Springer Nature Switzerland AG
9. Pooladvand K, Salerni AD, Furlong C (2020) In-situ thermal monitoring of printed components during rapid prototyping by fused deposition modeling. In: Residual Stress, Thermomechanics & Infrared Imaging and Inverse Problems, vol 6, pp 131–140
10. Bayle F, Doubenskaia M (2008) Selective laser melting process monitoring with high speed infra-red camera and pyrometer. In: SPIE - The International Society for Optical Engineering, Saint-Etienne. SPIE
11. Liu C, Law ACC, Roberson D, Kong Z (2019) Image analysis-based closed loop quality control for additive manufacturing with fused filament fabrication. J Manuf Syst 51:75–86
12. Altiparmak SC, Yardley VA, Shi Z, Lin J (2022) Extrusion-based additive manufacturing technologies: State of the art and future perspectives. J Manuf Process 83:607–636
13. Gibson I, Rosen D, Stucker B (2015) Additive manufacturing technologies, 2nd edn. Springer Science
14. Yanamandra K, Chen GL, Xu X, Mac G, Gupta N (2020) "Reverse engineering of additive manufactured composite part by toolpath reconstruction using imaging and machine learning," Composite. Sci Technol 198:108318
15. Wijnen B, Sanders P, Pearce JM (2018) Improved model and experimental validation of deformation in fused filament fabrication of polylactic acid. Prog Addit Manuf 3:193–203